Wear 269 (2010) 383–393

Contents lists available at ScienceDirect

Wear

journal homepage: www.elsevier.com/locate/wear

EBSD, SEM and FIB characterisation of subsurface deformation during tribocorrosion of stainless steel in sulphuric acid

J. Perret[a], E. Boehm-Courjault[b], M. Cantoni[c], S. Mischler[a,*], A. Beaudouin[d], W. Chitty[d], J.-P. Vernot[d]

[a] Ecole Polytechnique Fédérale de Lausanne (EPFL), TIC, Station 12, CH-1015 Lausanne, Switzerland
[b] Ecole Polytechnique Fédérale de Lausanne (EPFL), LSMX, Station 12, CH-1015 Lausanne, Switzerland
[c] Ecole Polytechnique Fédérale de Lausanne (EPFL), CIME, Station 12, CH-1015 Lausanne, Switzerland
[d] AREVA NP, Technical Center, F-71205 Le Creusot, France

ARTICLE INFO

Article history:
Received 26 January 2010
Received in revised form 9 April 2010
Accepted 22 April 2010
Available online 23 May 2010

Keywords:
Tribocorrosion
Plastic deformation
Passive films
Stainless steel
FIB
EBSD

ABSTRACT

The tribocorrosion behaviour of a 304L stainless steel/alumina contact was investigated in sulphuric acid at two imposed potentials (cathodic and passive). The metal deformation below the surface was investigated by analyzing cross sections using secondary electron microscopy (SEM) and electron back scatter diffraction (EBSD). Cross sections were also prepared using focussed ion beam (FIB) and analyzed by in situ SEM. AES depth profiling was used to analyze surface composition. Metal subsurface deformation resulted in the build up of a deformed layer of approximately 20 μm thickness in the near surface zone within the wear track. This layer exhibited a deformation gradient with high deformation close to the surface resulting in grain refinement down to 10 nm. The applied potential influenced the deformation: at passive applied potential more strain was accumulated below the surface resulting in more pronounced grain refinement and higher density of defects. Using AES analysis no alumina transfer from the counter body or any significant burying of oxide below the surface could be detected.

1. Introduction

Microstructural changes induced by plastic deformation of surfaces submitted to sliding play a crucial role for mechanical failure and wear of contacting materials. Plastic deformation can lead to failure by low cycle fatigue or by ratchetting involving strain accumulation in the material at each passes of the counter part [1]. New structures with properties differing from the substrate such as white layers or tribological transformed surface structures (TTS) form as a consequence of large plastic strain [2]. In tribocorrosion situations, material degradation proceeds by a combination of wear and corrosion [3]. In such situations, plastic deformation not only affects the mechanical failure by wear but also leads to the exposure of highly reactive bare metal and thus accelerates corrosion [3]. On the other hand, the mechanical response of the contacting metal can be profoundly affected by surface chemical reactions [4]. Further, strained structures may develop different electrochemical responses compared to the undeformed state [5]. It is therefore essential to gain more information on subsurface structural changes induced during tribocorrosion.

Structural modifications in the near surface region due to tribocorrosion were reported in the past. Buscher and Fischer [6] investigated using TEM surface microstructural modifications of CoCrMo alloys from hip joints after in vivo clinical use and after tribocorrosion on a laboratory device. In both cases they found a multi-layered structure including a top layer (approximately 1 μm thick layer) composed of granular nano-crystals (30 nm average diameter). Below this nano-crystalline layer these authors observed a deformed layer of complex structure. At depth between 1 and 10 μm a rather structureless deformed layer was identified. At lower depths plastic deformation resulted in the formation of stacking faults and ε martensite needles. Favero et al. [7] and Bidiville et al. [8] investigated the plastic behaviour of 316L stainless steel after sliding against a alumina in sulphuric acid under applied electrode potential. Those authors observed the formation of nano-crystalline structure in the near surface region. Interestingly, the extent of accumulated strain was found to depend on the applied electrode potential. In case of cathodic potentials, where the metal is in direct contact with the electrolyte, the nanograins had an austenitic structure with grain sizes around 160 nm. In case of passive potentials allowing for the formation of a nm thin surface oxide film, both austentic and α′ deformation martensite nanograins were observed with sizes of 40 and 20 nm, respectively. All these observation were in agreement with previously results obtained in dry conditions. Rigney [9] reported a layered surface

* Corresponding author. Tel.: +41 21 693 29 54; fax: +41 21 693 39 46.
E-mail address: stefano.mischler@epfl.ch (S. Mischler).

0043-1648/$ – see front matter © 2010 Elsevier B.V. All rights reserved.
doi:10.1016/j.wear.2010.04.023

structure formed on copper during sliding against hard steel. Using transmission electron microscopy (TEM) they found a 1 μm thick layer composed by nano-crystals (size well below 300 nm) covering the worn surface. This layer contains mixed material from the bulk as well as from the counterpart. The nanograins are partially oxidised. Below this layer the material exhibited a deformation gradient ranging from highly strained material at the interface with the nano-crystal layer to the undeformed bulk material. The strain resulted, depending on magnitude, in nano-sized refined grains (close to the surface) and dislocation cells which size increased with distance from the surface. A nomenclature was proposed [10] involving zones 1, 2 and 3 corresponding to the undeformed bulk material (1), the plastic gradient layer (2) and the mixed nano-crystal layer (3) at the surface, respectively.

Clearly the information available on microstructural modification induced by tribocorrosion is still very limited. One reason is the experimental difficulty in determining very fine microstructures on relatively large deformed samples. Most of the investigations were carried out by TEM, a technique implying tedious sample preparation work. In addition TEM analysis is very local and analysis of larger areas requires the preparation of a large number of samples. This study aims at characterising the deformation in the near surface region of materials submitted to tribocorrosion by using secondary electron microscopy (SEM) and electron backscatter diffraction (EBSD) of metallographic cross sections and SEM investigations of cross section formed in situ by using focussed ion beam (FIB). For this tribocorrosion samples were prepared by using a model contact involving an alumina ball sliding over a 304L stainless steel held at either cathodic or passive potential in sulphuric acid. The effect of normal load was evaluated. Micro-hardness and SEM were used to characterise hardness and surface topography of worn surfaces. Surface chemistry was analyzed using Auger depth profiling in order to identify possible chemical changes induced by rubbing.

2. Experimental

2.1. Material

The 304L austenitic stainless steel was supplied by AREVA NP. The composition, as determined by X-ray fluorescence spectrometry, was Cr 19.9%, Ni 10.6%, Mo 0.2%, Mn 2.5% and Fe balance. Average grain size was 26 μm. Samples were cut by spark erosion in form of disks of 20 mm diameter and 4 mm thickness. The discs were polished using emery paper and finally with 1 μm diamond particles using a Struers Abramin automatic polishing device. Samples were cleaned with ethanol in ultrasonic bath and stored in a dessicator. The test solution was 0.5 M H_2SO_4 prepared from p.a. grade sulphuric acid 95–97% and doubly distilled quality water. The counter pieces were alumina balls of 10 mm diameter AFBM grade 10 supplied by Saphirwerk (Brügg, CH).

2.2. Polarisation curve

Potentiodynamic polarisation curves were measured using a three-electrode set-up connected to an Autolab 30 potentiostat by sweeping the potential from −1.5 V up to 1 V at a rate of 2 mV/s. All potentials in this paper are given with respect to the saturated mercury sulphate reference electrode (MSE) which potential is 0.654 V versus the standard hydrogen electrode.

2.3. Auger electron spectroscopy

Auger depth profiling was performed with a Perkin-Elmer PHI 660 Scanning Auger Microprobe using a 2 keV argon ions gun. Primary electron beam potential and current were 10 kV and 20 nA, respectively. This resulted in an electron beam of less than 10 μm in diameter. The ion gun was rastered over an area of 1.5 mm × 1.5 mm. Under these conditions, the sputtering rate was 3 nm/min as calibrated with 30 nm Ta_2O_5 NPL standard.

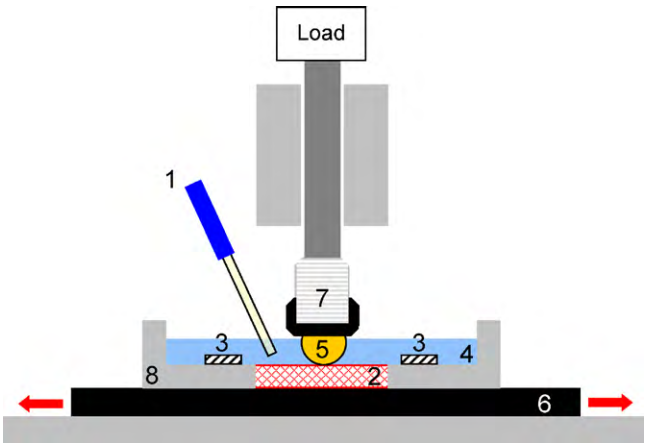

Fig. 1. Schematical cross section of the tribometer: 1: reference electrode MSE; 2: working electrode; 3: platinum counter electrode; 4: electrolyte; 5: alumina ball 10 mm diameter; 6: linear stage; 7: two-dimensional force sensor; 8: electrochemical cell.

2.4. Tribometer

The tribocorrosion tests were carried out using a reciprocating tribometer using a ball (alumina) on flat (304L steel) configuration. The tribometer is schematically shown in Fig. 1. The 304L steel is mounted on an PVC electrochemical cell (volume 30 ml) fixed on an Aerotech ALS130-050 linear motor stage. A Soloist CP20 device connected to a PC controls motion of the latter. The disk area exposed to the solution is 2.5 cm^2.

The alumina ball is fixed on the lower end of a shaft maintained vertically by a linear ball bearing. The load is applied through the positioning of appropriate masses on the upper end of the shaft. The ball holder includes a two-dimensional piezo-resistive force transducer manufactured by Reznicek & Hlach. The force transducer was connected to two HBM MC55 amplifiers controlled by an AB12 display unit. The stainless steel disk was connected as working electrode to a Bank LB94AR potentiostat together with a saturated mercury sulphate reference electrode (MSE) and a coiled platinum wire serving as counter electrode. The reference electrode was positioned 3 mm above the sample plate at a distance of approximately 5 mm from the wear track.

A desktop computer equipped with a PCI6034 National Instruments data acquisition board running under LabView7 software provides control of the system and data acquisition. The typical sampling rate is 1 kHz per channel. This system permits the simultaneous acquisition of the following parameters: the normal force, the tangential force, the applied potential and the current. The coefficient of friction was determined by dividing the frictional and normal forces when the ball was in the middle of the wear track.

2.5. Tribotests

Two different electrochemical treatments were considered. In cathodic experiments the sample, after having being mounted in the tribometer electrochemical cell containing the electrolyte, was first pre-polarised at a cathodic potential of −1.8 V for 5 min in order to clean the surface. Subsequently, the potential was brought to a cathodic value of −1 V. Immediately after, rubbing was started while maintaining the applied potential. In passive experiments

the sample was cleaned for 5 min at −1.8 V, left at open circuit potential for 5 min and subsequently polarised at a passive potential of −0.5 V. Rubbing was started 15 min after applying the passive potential. The applied potential was maintained while rubbing.

The normal load for passive conditions was 7 or 24 N corresponding to an average Hertzian pressure of 676 and 1020 MPa, respectively. The contact pressure is much higher than the steel yield strength (approximately 200 MPa) and thus the contact is expected to behave plastically. The cathodic tests were carried out only at 7 N applied load. All experiments were carried out at room temperature (21–22 °C). The linear motor imposed a reciprocating motion of 1 Hz frequency and 5 mm amplitude. Rubbing duration was 1800 s corresponding to a sliding distance of 18 m. At the end of the test the discs and the balls were removed from the solution and rinsed with distilled water. For each condition the experiments were repeated three times.

The volume of the wear track was quantified using non-contact scanning laser profilometry (UBM Telefokus Instrument). The average cross section was determined for three profiles across the wear track for each sample at one-fourth, one-half and three-fourth of the track length. Wear volume was obtained by multiplying the average cross section by the track's length. 304L steel microhardness was measured for the samples exposed to all potentials inside and outside the wear tracks using a Leitz Weitzlar 721 300 device. Applied load was 200 × *g* during 15 s.

2.6. Cross section preparation for SEM and EBSD

The worn samples were cut using a diamond wire saw (Well model 3032-4) perpendicularly to the wear track and approximately in the centre of it. The worn side of each sample was protected by a Technovit 5000 PMMA resin (Heraeus Kulzer GmbH) coating. This 1–2-mm thin layer was intended to prevent the edges rounding during mechanical polishing. The samples were then mounted in a thermoplastic resin ("Konductomet", Buehler) and ground with a Struers Abramin automatic polishing device. Increasingly fine SiC papers (from grade 220 to 2400) with water as a lubricant were first used. Finally, mirror quality surface finishing was achieved using 6- and 1-μm diamond sprays.

Two different final steps of preparation were applied depending on the analytical techniques to be used. For EBSD observation the final polishing was manually performed during 25 min using a Struers "OP-S" silica suspension in which 7 vol.% of hydrogen peroxide (30%) was added. This final preparation was performed to remove the mechanically deformed thin surface layer and thus to obtain well-contrasted, easily indexable EBSD patterns, at least in the unworn area. For SEM analysis (Philips XL30 apparatus) the mirror polished cross sections were electrochemically etched in 10 vol.% oxalic acid (6 V, 20 s) in order to reveal the microstructure.

2.7. EBSD measurement

The EBSD analyses were performed using a XL30FEG scanning electron microscope (Philips Electronics Instruments Corp., Mahwah, NJ, USA), equipped with a Nordlys I detector (HKL Technology A/S). The HKL Channel 5 software was used for acquisition and treatment of data. Measurements were done using following parameters: tilt of 70°, accelerating voltage of 25 kV, spot size of less than 10 nm and working distance selected between 17 and 19 mm. The measurement step size was 0.5 μm. Two phases were indexed, austenite (fcc) and ferrite (bcc) according to the HKL phases database concerning this type of steel. The ferrite phase corresponds to residual ferrite formed during steel processing and/or to the phase transformation from austenite to α′ deformation martensite. To reduce indexing errors, the indexation procedure was set so that at least 10 bands were detected and simulated on the EBSD patterns.

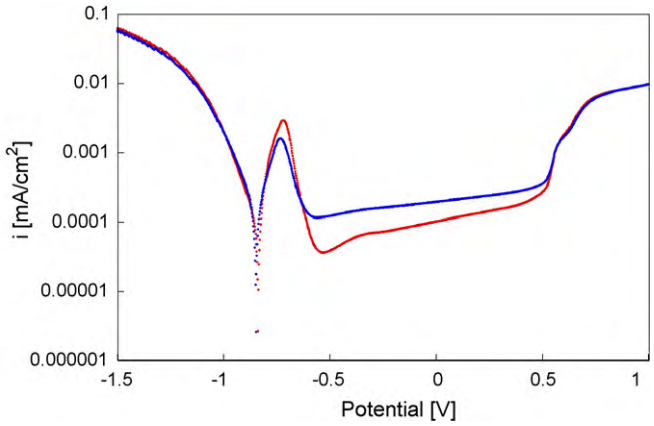

Fig. 2. Potentiodynamic polarisation curve of the 304L steel in 0.5 M sulphuric acid. The results of two independent tests are plotted.

2.8. FIB measurement

Deformed zone were observed with a Zeiss NVision 40 Cross Beam system incorporating a focused ion beam (FIB) and a high-resolution field emission SEM. The gallium liquid metal ion source polishing allowed to mill, polish and deposit. Cross beam microscopy allowed live SEM imaging during milling, polishing and deposition. The microscope is equipped with a standard Everhart-Thornley secondary electron (SE) detector and an in-lens detector (Zeiss Gemini column). The electron beam conditions were optimised for grain contrast with an accelerating voltage of 1.7–1.9 kV and a beam current of 1 nA approximately. The observations were realised using the in-lens detector with a 60 μm aperture. A tilt compensation of 36° was applied to correct the images for the angle between analyzed surface and incident electron beam. Prior to milling, a protective carbon layer of about 1 μm thickness was deposited by ion beam induced deposition on an area of 20 μm × 10 μm on the worn surface. A trench was cut in front of the deposited area by scanning the vertical (with respect to the sample surface) ion beam (13 nA, 30 kV) over a trapezoidal area. The scan was started 25 μm away from the deposit to generate a ramp like trench. When approaching the deposit edge the width of the scan was continuously reduced from 50 to 25 μm (trapezoidal area). Once the edge of the deposit was reached the ion current was reduced first to 6.5 nA and further to 0.7 nA in order to obtain a as smooth as possible surface for SEM analysis and to avoid artefacts such as curtaining.

3. Results

3.1. Electrochemical behaviour

Fig. 2 represents the polarisation curves of the investigated 304L steel measured in sulphuric acid. Four potential regions can be distinguished. Below the corrosion potential (−0.85 V) the current is negative and controlled by the cathodic reduction of protons. In the anodic domain, an active peak is observed between the corrosion potential and the potential of −0.56 V above which a passive plateau appears. The transpassive potential of 0.51 V limits the passive plateau at high potential. The potentials chosen for tribological tests (−1 and −0.5 V) lie in the cathodic domain and in the passive plateau, respectively.

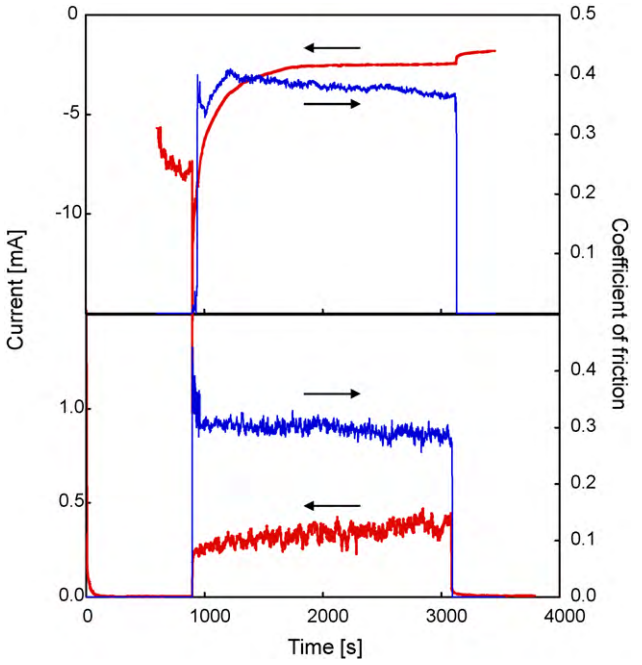

Fig. 3. Tribocorrosion test I, μ vs. time at cathodic −1 V and passive −0.5 V potential and load 7 N.

3.2. Tribocorrosion behaviour

The typical evolution of the current and the coefficient of friction are illustrated in Fig. 3 for the cathodic and the passive potentials. Rubbing little affects the current in the cathodic domain as evidenced by the small change occurring at the end of rubbing. Note that the decrease in current observed at a time of 900 s in Fig. 3 is likely related to the potential step from −1.8 to 1 V imposed just before the onset of rubbing. At the passive potential, the onset of rubbing corresponds to a sudden enhancement of the current due to the abrasion of the passive film. During rubbing the current drifts to higher values probably because the rubbed area increases with the progress of wear. At both potentials the coefficient of friction attains quickly a steady state value. The average value of the coefficient of friction during rubbing is reported in Table 1 together with the average value of the anodic current $I_{rubbing}$ measured during rubbing at the passive potential.

Fig. 4 shows typical cross section scans measured by laser profilometry across the wear scars formed on the steel. Larger wear is observed at the passive potential where ridges form at the track edges. The surface of the wear track is smoother at cathodic potential. The wear volumes listed in Table 1 were extracted from the cross sections profiles by multiplying the wear track length by the difference between the cross section area of the track and the total cross section area of the ridges. Wear is highest at passive potential under a load of 24 N. No wear or any other damage could be observed using optical microscopy on the alumina balls after wear test.

The steel worn surface topography was investigated using SEM (Fig. 5). The wear track formed at the cathodic potential is characterised by a relatively smooth appearance and finer scratches. At passive potentials larger scratches are present. At higher load the wear scar at passive potential exhibits deep scratches and large deformation ridges. Table 2 reports the micro-hardness values measured inside the wear track. Outside the wear track, independently on potential the micro-hardness was 140 ± 11 HV. Table 2 shows that the rubbed surface work-harden more markedly at passive potential.

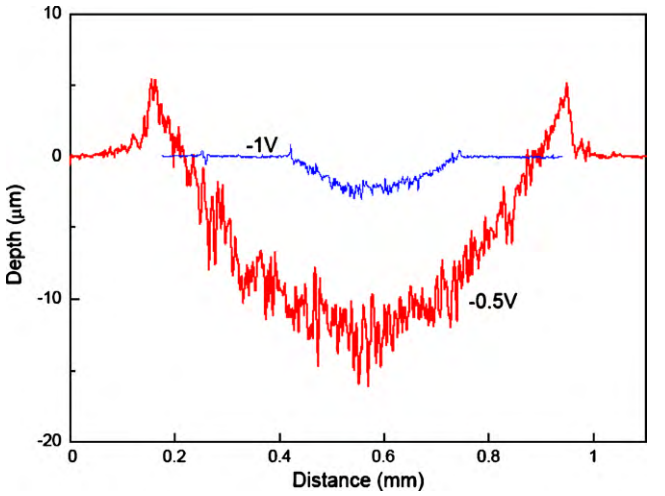

Fig. 4. Cross section profile of the wear track formed on 304L SS after rubbing against a smooth alumina ball in 0.5 M H_2SO_4 at cathodic potential −1 V and at passive potential −0.5 V and normal load of 7 N.

Table 2
Micro-hardness inside the wear scars.

Potential, load	Vickers micro-hardness (200 g)
−1 V, 7 N	182 ± 38
−0.5 V, 7 N	319 ± 18
−0.5 V, 24 N	344 ± 7

Average and standard deviation of three independent tests for each condition.

3.3. Surface composition

AES analysis was carried out on worn and unworn surfaces. No aluminium signals could be detected thus indicating the absence during rubbing of material transfer from the counter piece to the stainless steel. Fig. 6 shows the depth profiles measured outside (Fig. 6a) and inside (Fig. 6b) the wear track after a tribocorrosion experiment at imposed passive potential (−0.5 V) as well as a depth profile measured inside the wear track formed under an applied cathodic potential (Fig. 6c). Fig. 6a indicates the presence of a approximately 1.5 nm thin surface oxide film whose thickness corresponds well with data for passive film on this type of steel [11]. Inside the wear track the oxide film appears much thicker (Fig. 6b). This can be due to a mixing or burying of the surface passive film as a consequence of surface strain of the metal or also to an artefact induced by the high roughness of the wear scar. Under applied cathodic potential, surface oxide films cannot form. The oxide film observed in Fig. 6c forms after the tribotest during washing of the

Table 1
Effect of potential on load, friction, anodic current and wear.

Potential (V)	Normal force (N)	Coefficient of friction	$I_{rubbing}$ (mA)	Wear volume (mm^3)
−1	7	0.37 ± 0.01	–	0.003 ± 0.0003
−0.5	7	0.32 ± 0.02	0.33 ± 0.02	0.023 ± 0.002
−0.5	24	0.35 ± 0.01	0.68 ± 0.08	0.051 ± 0.002

Average and standard deviation of three independent tests for each condition.

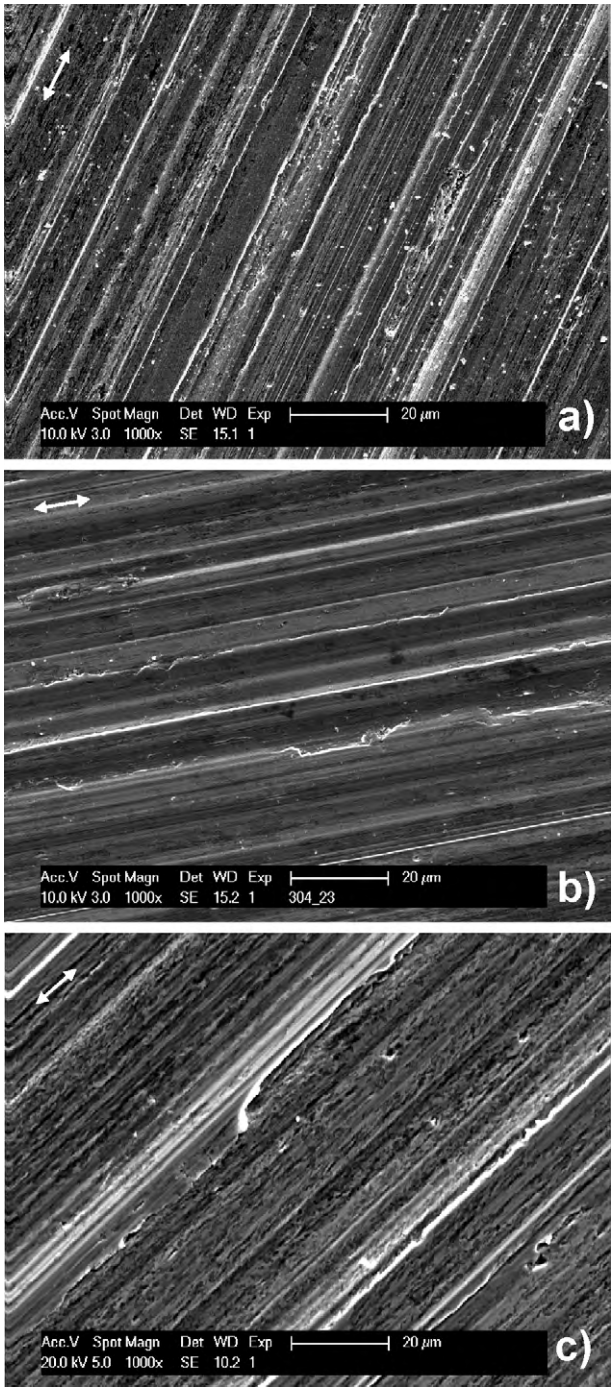

Fig. 5. SEM images taken in the centre of the wear tracks formed at (a) cathodic potential, 7 N normal force, (b) passive potential, 7 N normal force and (c) passive potential, 24 N normal force. Arrows indicate sliding direction.

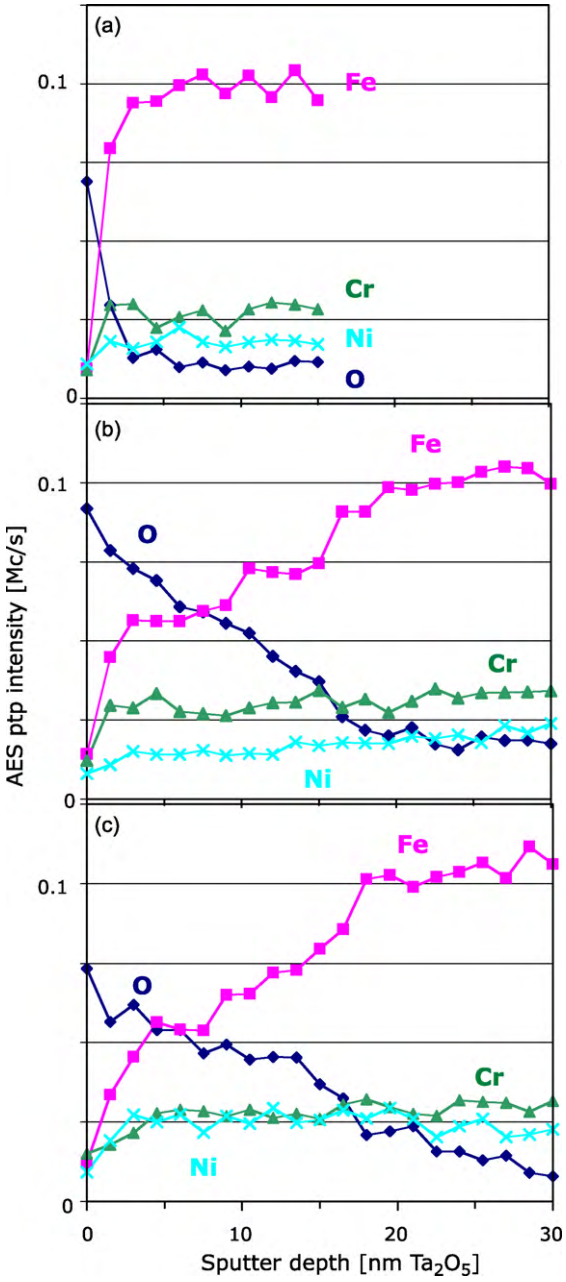

Fig. 6. AES depth profiles measured on (a) passive surface, outside of the wear track, (b) wear track formed at passive potential (7 N normal force) and (c) wear track formed at cathodic potential (7 N normal force).

sample with water and storage in air before analysis. The fact that the cathodic depth profile exhibits a similar slow decrease of the oxygen signal with depth as under applied passive potential indicates that the apparent thickening of the oxide film inside the wear track is rather related to a roughness artefact than to a tribological effect.

3.4. SEM cross sections

Typical SEM images taken after etching cross section polished samples are shown in Fig. 7. The original grain structure of the stainless steel is clearly visible in the cross sections taken on areas not subject to rubbing (Fig. 7a). Grain boundaries are clearly distinguishable even when they reach the surface. On cathodic samples (Fig. 7b) one can observe a very thin (less than 1 μm) etched layer at the outermost surface as well as some stripes, also located close to the surface, indicating twins formation. Grain boundaries do not reach the surface but ends at the edges of the etched layer. The etched layer is significantly thicker in samples rubbed at the passive potentials (Fig. 7c and d) where it reaches an approximate thickness of 10–20 μm for a load of 7 N and 20–30 μm for a load of 24 N. Note that the thickness of the etched layer is not homogeneous and varies from grain to grain. It seems also that etching is confined within the grains exposed to the surface. The grain marked with an asterisk does not reach the surface and does not exhibit etching although the grains located close by at the same depth exhibit

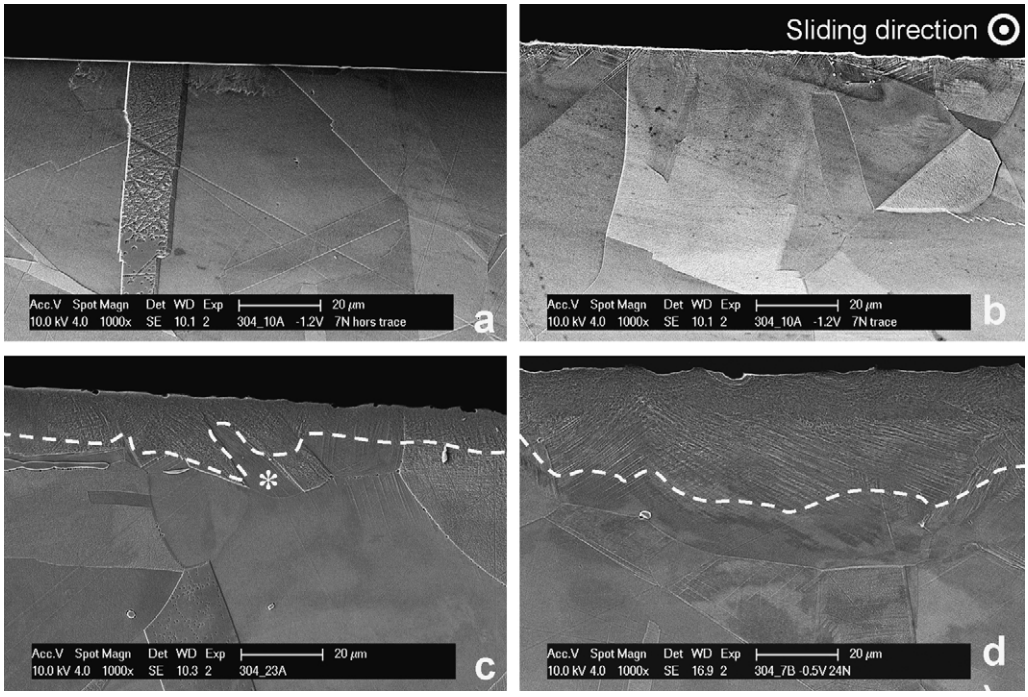

Fig. 7. SEM cross section (a) out of the wear track, (b) cathodic potential, 7 N normal force, (c) passive potential, 7 N normal force and (d) passive potential, 24 N normal force.

attack. Note however, that etching is a corrosion process that is usually strongly influenced not only by the strain in the metal but also by grain orientation. The presence of twins is more marked in the samples worn at higher load.

3.5. EBSD cross sections

Fig. 8 shows different views obtained with the EBSD instrument of the cross section of a sample rubbed at passive potential under a load of 7 N. The cross section includes the full width of the wear scar as well as its edges. Fig. 8a represents the SEM image. Despite the limited resolution due to the large primary beam current used in EBSD this image allows to identify the frontier between the sample surface and the resin mount. One can also distinguish the unworn area, the ridges as well as the wear track area. Fig. 8b shows the results of the phase indexation with the fcc phase marked in red and the bcc phase marked in blue. For comparison purpose the frontier of the sample surface determined on the SEM image was superposed to the phase indexation map. Clearly, the software could not index an approximately 5–10 μm thick surface layer extending over the entire wear track width. Interestingly, this layer corresponds to the etched layer visible in Fig. 7c. The diffraction patterns taken at different depths below the worn surface are shown in Fig. 9. At a depth of 5 μm below the surface the Kikuchi lines (Fig. 9) are clearly visible and could be indexed using the imposed procedure. The diffraction pattern taken at 3 and 4 μm below the surface is very similar to the previous one (5 μm) but could not be correctly indexed because of lattice distortion. This indicates that at this depth the fcc structure was highly deformed. No Kikuchi lines can be identified in the near surface region down to a depth

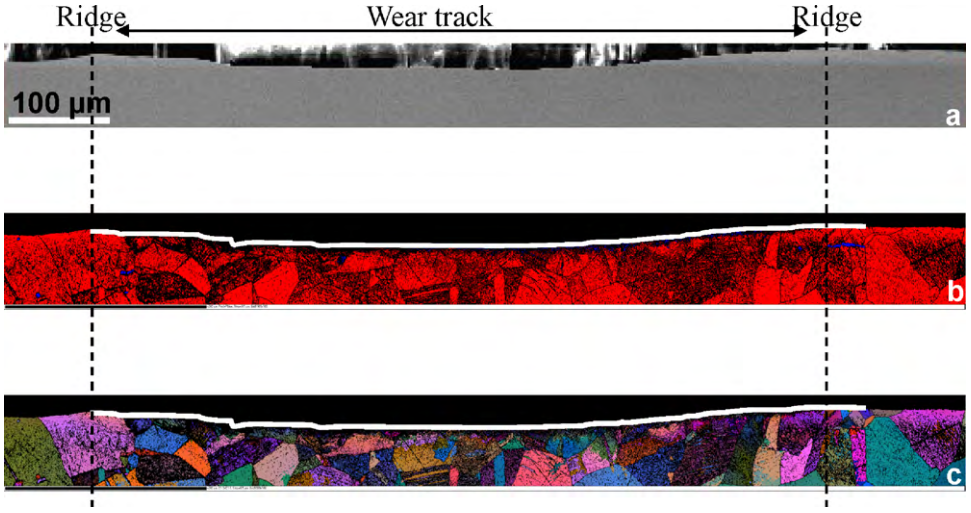

Fig. 8. EBSD analysis in the subsurface of the wear track after tribocorrosion test at passive conditions −0.5 V and 7 N load. (a) SEM image; (b) phase indexation (red fcc phase–blue bcc phase); (c) Euler representation. The white lines in (b) and (c) show the sample surface as observed in the secondary electron image (a). (For interpretation of the references to colour in this figure legend, the reader is referred to the web version of the article.)

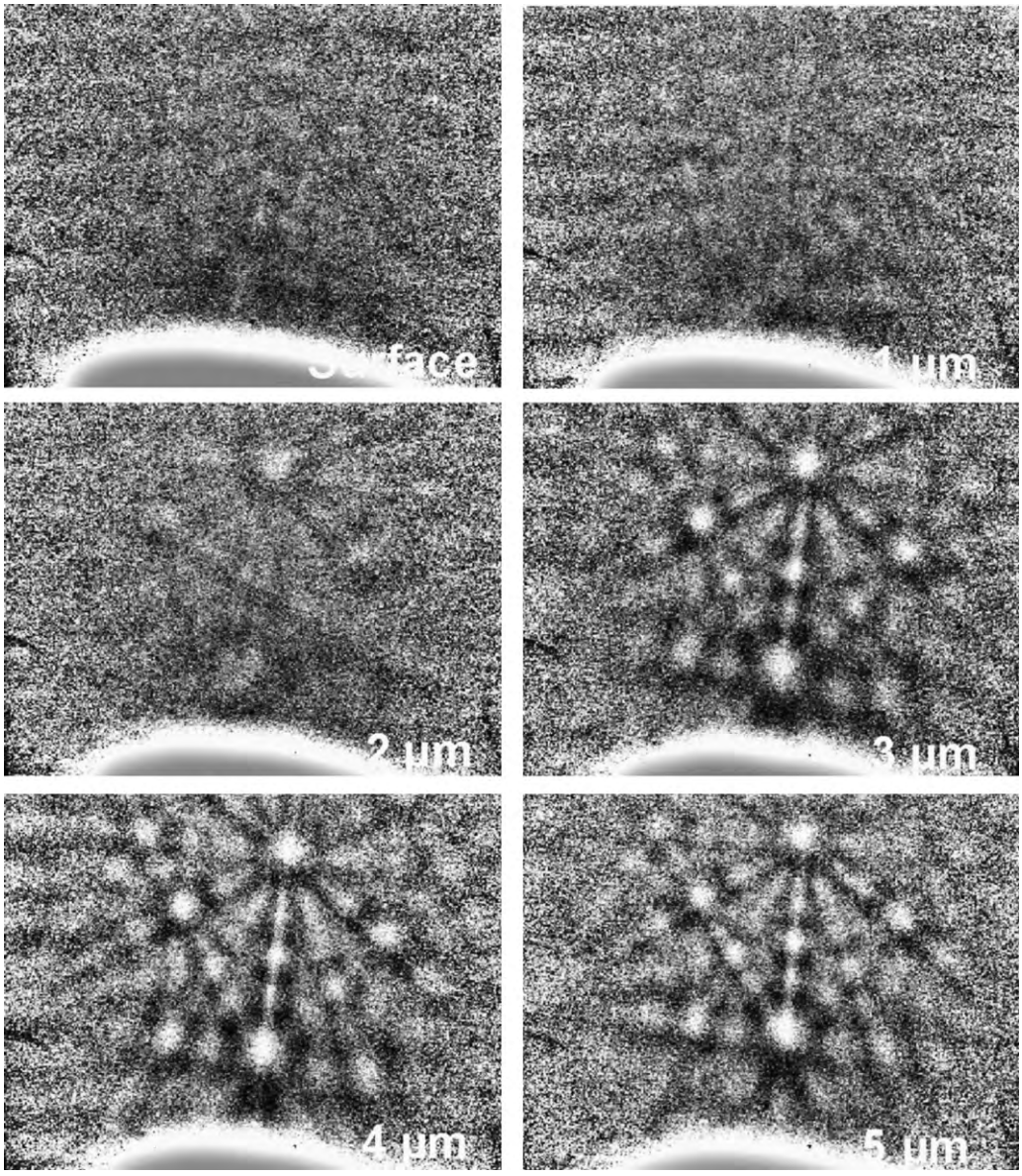

Fig. 9. Diffraction patterns in the subsurface of the wear track of a tribocorrosion test in passive conditions. Only diffraction patterns at depth higher than 4 μm could be indexed.

of 3 μm. This appearance can be explained by two possible phenomena. First, the size of the diffracting grains is smaller than the primary electron beam diameter (1 μm). Secondly, the metal structure can be so distorted that diffraction is suppressed. Most of the indexed phase corresponds to austenite, only isolated spots of the bcc phase are found in particular close to the surface. This latter cubic phase corresponds in principle to α′ deformation martensite.

Fig. 8c represents the grain orientation in a colour scale. Well-defined grains with homogeneous orientation and clear defined boundaries are observed outside the wear track and within the wear track but only well below the surface. The orientation of the grains touching the worn surface is not well defined probably because subgrains of different orientation form here as a consequence of heavy deformation.

Fig. 10 shows EBSD cross sections of wear tracks formed at cathodic and passive potential. At cathodic potential the indexation in fcc phase could be carried out up to the outermost surface while in the passive film an unindexable layer appears. This is consistent with the SEM cross sections showing little or no etched layer at cathodic potential.

3.6. FIB cross sections

Fig. 11 shows a cross section prepared through FIB of wear tracks formed at passive (Fig. 11a) and cathodic potential (Fig. 11b). The analyzed areas are always located in the centre of the wear track. The contrast is due to electron channelling effects dependent of grain orientation. A surface layer formed by grains of much finer size than the bulk material (30 μm grain size) is clearly visible in Fig. 11a and b. Clearly a grain refinement has taken place during tribocorrosion due to large shear strain acting in the contact. Indeed similar grain refinement is found in severe plastic deformation processes [12]. Emge et al. [13] found similar structures after sliding on copper by using ion channelling on FIB sections. The thickness of the tribologically grain refined (TGR) layer varies depending on location on Fig. 11a between 3 and 4 μm (right) to 7–8 μm (left). At cathodic potential the TGR layer is confined within the first μm below the surface (Fig. 11b). Below the TGR layer the original grain structure can be observed with locally some twin formation.

In order to determine the refined grain size, lines were plotted parallel to the surface at different depths below the surface

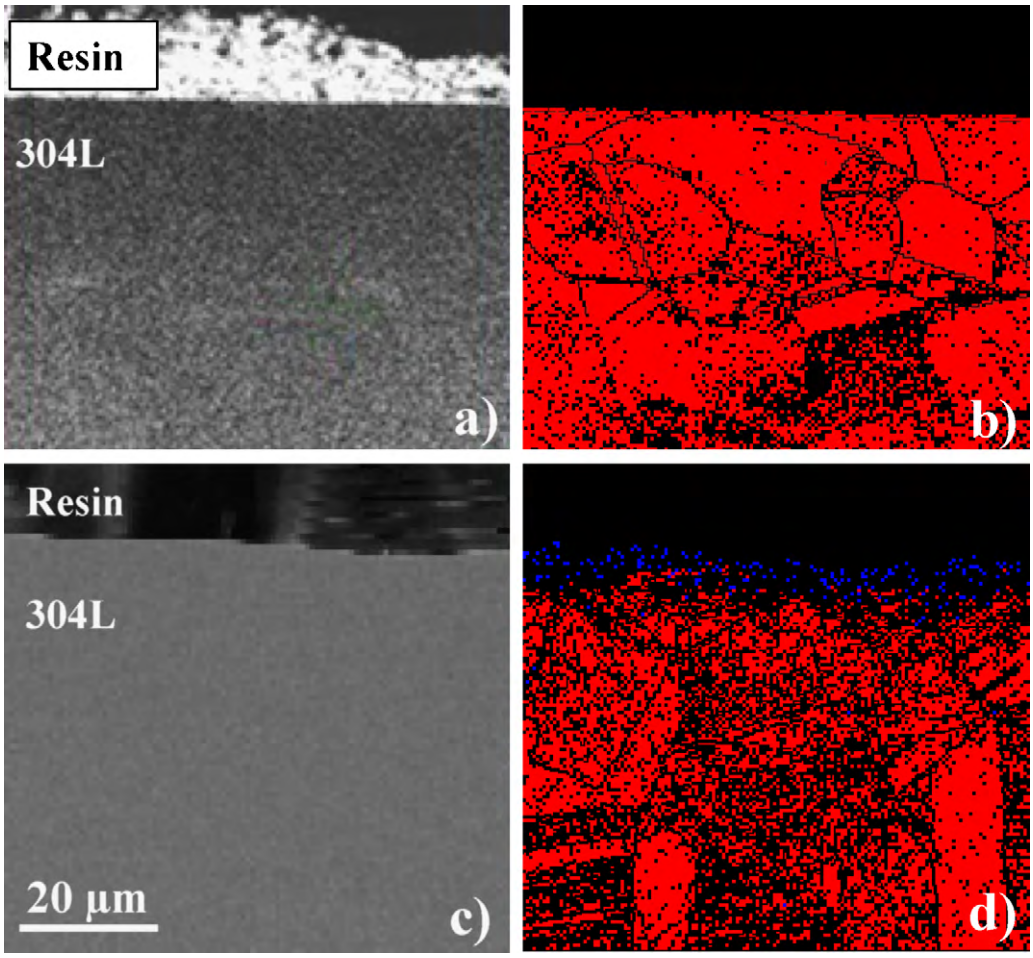

Fig. 10. EBSD analysis. SEM image and phase indexation (red fcc phase–blue bcc phase) in the subsurface of the wear track after tribocorrosion test: (a and b) cathodic conditions −1 V and 7 N; (c and d) passive conditions −0.5 V and 7 N. (For interpretation of the references to colour in this figure legend, the reader is referred to the web version of the article.)

on the FIB cross section micrographs. The grain size was determined as the ratio between the line length (8–10 μm) and the number of intersection points between line and grain boundaries (identified as boundaries between domains of different grey tone intensity). The operation was repeated on two different locations of the same micrograph for the cathodic and passive potential (Fig. 11a and b). The obtained data are plotted as a function of depth in Fig. 12. Despite some uncertainties in the precise identification of grain boundaries in grey tone images reproducibility is reasonably good and allows one to distinguish different grain size distribution depending on potential. At cathodic potential the grain size at the surface is approximately 0.15 μm. The grain size increases continuously with depth following an exponential trend. The change in grain size with depth is slightly different at passive potential and is characterised by an abrupt change in gradient at approximately 5 μm depth. Close to the surface only small increase in size from 0.15 to 0.34 μm occurs while above 5 μm depth a rapid increase in the grain size is observed.

Fig. 13 shows a longitudinal (parallel to the sliding direction) of the wear track formed at passive potential. A similar TGR layer is also observed here. The shape of the refined grains close to the bulk material is rather isometric while the grains become more needle like when approaching the surface. Moreover, close to the surface the needle like grains seem to be bended towards the sliding direction. This suggests that grains tend to align themselves along the direction of sliding. Note however that under reciprocating motion the direction of sliding changes at each stroke. Thus the alignment observed in Fig. 13 could result only from the last stroke. This would suggest that the TGR layer is highly deformable. On the other hand, it is also conceivable that alignment results from the very first stroke when contact pressure is high and significant ploughing occurs.

4. Discussion

4.1. Comparison of techniques

The results of the SEM, EBSD and FIB/SEM analyses yield a consistent picture of the subsurface deformation occurring during tribocorrosion. In SEM cross sections subsurface deformation is revealed by the preferential dissolution of regions with high density of defects (such as vacancies, interstitial atoms, dislocations). The thickness of the etched layer (Fig. 7c) varies between 10 and 20 μm approximately at passive potentials while at cathodic potential the thickness is less than 1 μm. As expected, the deformation and thickness of the etched layer increase at higher loads. SEM observation of the FIB cross sections reveals the presence of a grain refined layer with a thickness of 3–8 μm. This reduction in grain size was attributed to a dynamic recrystallisation process taking place during deformation and triggered by the very high degree of deformation [6]. It corresponds well to microstructures observed after severe plastic deformation for which models were proposed based on conversion of homogenous dislocation distributions into more energetically favourable subgrains. Favero et al. [7]

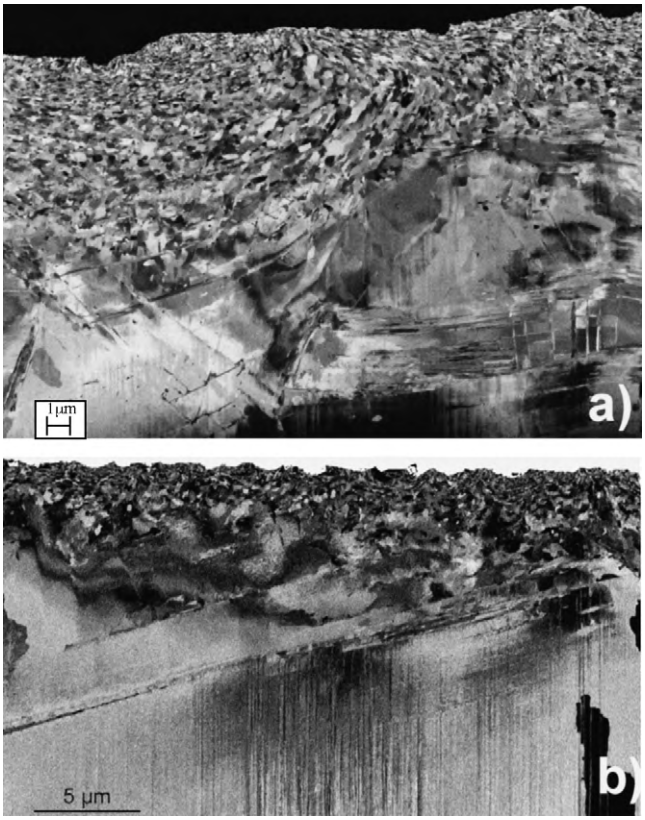

Fig. 11. FIB transversal cross section of wear track formed at (a) passive potential −0.5 V and (b) cathodic potential −1 V (both at 7 N load).

and Bidiville et al. [8] also deduced from TEM patterns the formation of nanograins in stainless steel after sliding in sulphuric acid. Although nanograins of less than 70 nm diameter were observed close to the worn surface in Fig. 11 the average grain size is much larger than the one reported by Bidiville et al. [8] (40 nm). At this stage it is not clear if these differences have to be ascribed to the different materials investigated, the different tribological conditions or the differences in analytical techniques.

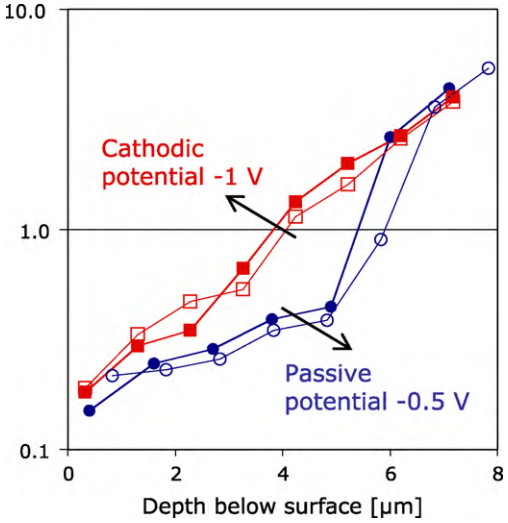

Fig. 12. Evolution of the grain size with depth under the surface. Circles and squares correspond to passive and cathodic potentials, respectively. Two sets of data were extracted from two locations in Fig. 11a and b for each potential.

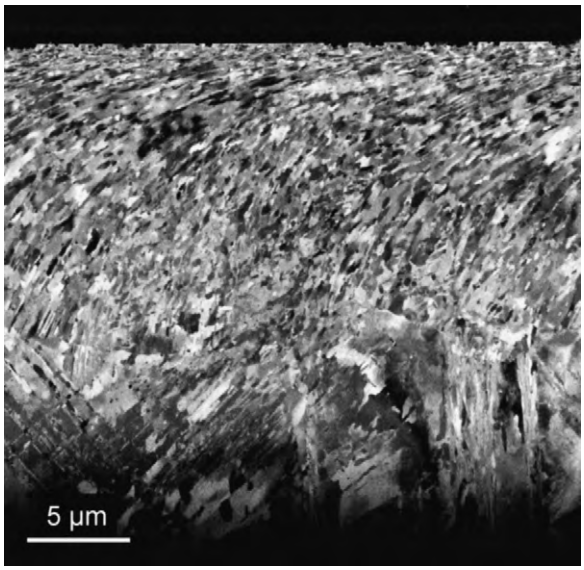

Fig. 13. Longitudinal cross section of wear track formed at the passive potential under a load of 7 N.

Structures composed by grains smaller than the diameter of the electron beam used for EBSD (less than 1 µm) do not yield well-defined diffraction patterns since several crystallites contribute to diffraction. Accordingly, EBSD analysis shows the existence of a non-indexed layer which thickness (5–10 µm) corresponding well with the tribological grain refined layer observed in FIB. The thickness of the etched layer is however larger than the TGR layer. This indicates that the metal below the nano-crystalline layer was also deformed although to a lesser extent than at the surface. Indeed, parallel lines in the FIB cross section (Fig. 11) indicate the presence of deformation twins in the zone below the TGR layer. Metallographic SEM sections also show a large number of twins below the etched layer (Fig. 7c and d).

4.2. Near surface structure

Three subsurface zones are typically observed after wear: the undeformed bulk material (zone 1), the plastic deformed layer with strain gradient (zone 2) and the mixed nano-crystalline surface layer (zone 3). The present results do not yield evidence for the presence of zone 3. Indeed the AES analysis does not show either transfer of alumina of the steel or subsurface oxidation. The zone 2 is clearly identified where the increasing deformation from the surface to the bulk manifest itself by the grain refinement at the surface and the presence of twins in the region close to the bulk alloy. Thus zone 2 includes the TGR layer observed in the FIB cross sections as well as the etched layer observed on metallographic samples. Indeed, Fig. 11 indicates a continuous decrease of the grain size with depth suggesting an exponential decrease of strain from the surface towards the bulk alloy as reported in previous papers [9]. The increase in grain size observed in Fig. 12 should reach a limit corresponding to the grain size of the bulk material. Extrapolating the graph in Fig. 12 to the grain size of the bulk material (26 µm) one obtain a depth of 12–15 µm. This value corresponds well with the thickness of the etched layer observed at passive potential (between 10 and 20 µm) but largely exceeds the thickness observed at cathodic potential (1 µm). This suggests that the refined grains formed at passive potential contain more defects that the corresponding grains formed at cathodic potential. This is in agreement with the larger micro-hardness values measured at passive potential.

4.3. Effect of potential

The samples rubbed at cathodic potential exhibit clearly less deformation that the ones tested at passive potential, and this for the same number of cycles. Indeed, only a thin etched layer can be observed in the SEM images and indexation by EBSD analysis could be achieved up to the surface of cathodic samples. Further evidence is given by the micro-hardness measurements inside the wear scar (Table 2) that show significant more work-hardening at passive potential. Favero et al. [7] and Bidiville et al. [8] already observed larger strain accumulation at passive potential through subsurface TEM analysis of 316L steel after tribocorrosion tests in sulphuric acid.

Strain accumulation depends in principle on the stress field acting in the contact as well as on material properties. In the present case friction is quite independent on applied potential (Table 1) and thus cannot account for the different deformation behaviour. The normal load distribution may slightly vary due to different geometry of the wear scar. Under this hypothesis one would expect higher pressure and larger accumulated strain at cathodic potential since by equal load the wear track is smaller compared to passive conditions. This is however not the case here.

Strain accumulation and dynamic recrystallisation are closely related to the amount and mobility of dislocations. The frictional shear stress acting at the metal surface generates dislocations. The maximum of the shear stress is located right at the outermost surface since the coefficient of friction exceeds 0.3 [9] in the present experiments. Thus dislocations generated at the surface either diffuse towards the bulk of the steel or are annihilated when emerging at the metal surface. However, the presence of a passive film can reduce or even suppress dislocation annihilation by blocking the metal surface [14]. Thus the flux of dislocation towards the bulk material is enhanced leading to higher dislocations densities in the subsurface and favouring dynamic recrystallisation into smaller grains over larger depths. Such phenomena are effectively observed in the present study. The observation that the etched layer is confined to the grains emerging to the surface, independently on depth, suggests that diffusion of dislocations can be stopped by grain boundaries and thus also by surface oxide films which are similar defects as grain interfaces.

Note that the barrier effect of a passive film may depend in principle on several factors [7]: differences in elastic properties between metal and oxide film, mismatch of oxide and metal lattice, and internal stresses generated during film formation. Further, the cationic stoichiometry of the passive films usually does not match exactly the alloy composition. Thus the metal layer underneath the passive film may undergo compositional changes during passivation that can lead to changes in critical properties for dislocation mobility such as the stacking fault energy. The consequences of the barrier effect on the strain accumulation are also quite complex as they involve specific mechanisms of dislocation movement, the capability of the metal to work-harden and to create cells and subgrains.

4.4. Microstructure and wear

The relation between microstructure and wear is still a matter of debate. According to classical wear models [1] wear occurs when the sliding material has accumulated by ratchetting or low cycle fatigue a critical amount of strain (strain to failure). In the present case, one would therefore expect more mechanical wear at passive potential where more strain is globally accumulated in the metal surface. However, no evidence of subsurface fatigue cracking could be found with the techniques used in this study.

Recently it has been proposed [6,9] that wear arises from the detachment of nano-crystals from the sliding surface and not by subsurface rupture as postulated in fatigue wear theories. The grain size at the metal surface is similar so that one would expect the same mechanical behaviour and thus the same mechanical wear independently on potential.

To identify the acting wear mechanisms one would need to quantitatively distinguish between metal that was detached as particle (mechanical wear) and metal that was oxidised during rubbing (wear activated corrosion). At cathodic potential the contribution of wear activated corrosion to the overall wear is in principle negligible and thus the wear volume corresponds to the mechanical wear. Corrosion clearly acts at passive potential as indicated by the increase in current observed during rubbing (Fig. 2). The increase in current can be converted in anodic volume, i.e. the equivalent metal volume that was corroded during rubbing, using Faraday's law. The details of the calculation are discussed in reference [7]. This conversion requires the knowledge of the valence of dissolution of each alloy component. However, in the present case only the oxidation valence of Cr and Ni can be reasonably assumed to be 3 and 2, respectively. For iron there is an uncertainty because values of 2 and 3 are both plausible [15]. This implies that the anodic volume varies between 0.020 mm^3 (Fe valence 2) and 0.014 mm^3 (Fe valence 3) (the contribution of minor alloying elements was neglected). The volume removed by mechanical wear corresponds to the difference between total wear volume (Table 1) and anodic volume. According to this one obtains mechanical wear volumes of 0.03 mm^3 (Fe valence 2) and 0.09 mm^3 (Fe valence 3). The former value is similar to the wear volume found at cathodic potential while the second value is significantly larger. Clearly the uncertainty in the valence of oxidation does not allow concluding about possible differences in mechanical wear linked to the applied potential and the accumulated strain.

5. Conclusions

The SEM and EBSD analysis of metallographical and FIB cross sections as well as the Auger surface analysis of wear tracks formed during tribocorrosion of stainless steel have shown that:

- A plastically deformed layer develops underneath the rubbed surface. Deformation manifests itself by grain refinement with an exponential decrease in grain size from nanograins (100–200 nm in diameter) at the surface up to the bulk grain size (26 μm) approximately 15 μm below the surface. The FIB cross sections suggest that subsurface materials flow occurs within the grain refined layer. The presence of structural defects revealed by electrochemical etching constitutes another appearance of deformation that overlaps with grain refinement.
- No evidence for subsurface cracking could be found. No significant material transfer from the counter piece nor embedding of oxides could be detected using Auger electron spectroscopy on the steel surface.
- The extent and nature of deformation depends on the electrochemical conditions prevailing during tribocorrosion. More strain is accumulated when the passive potential is applied during rubbing. This results in a thicker grain refined layer with finer grains extending deeper below the surface and a larger density of defects. This effect is attributed to the barrier effect exerted by the passive film that inhibits annihilation of dislocation emerging at free surfaces.

Acknowledgement

The authors are grateful to N. Xanthopoulos, EPFL-CIME for AES surface analysis.

References

[1] A. Kapoor, F.J. Franklin, Tribological layers and the wear of ductile materials, Wear 245 (2000) 204–215.
[2] E. Sauger, S. Fouvry, L. Ponsonnet, Ph. Kapsa, J.M. Martin, L. Vincent, Tribologically transformed structure in fretting, Wear 245 (2000) 39–52.
[3] D. Landolt, S. Mischler, M. Stemp, S. Barril, Third body effects and material fluxes in tribocorrosion systems involving a sliding contact, Wear 256 (2004) 517–524.
[4] J. Stojadinovic, L. Mendia, D. Bouvet, M. Declercq, S. Mischler, Electrochemically controlled wear transitions in the tribocorrosion of ruthenium, Wear 267 (2009) 186–194.
[5] V. Vignal, N. Mary, P. Ponthiaux, F. Wenger, Influence of friction on the local mechanical and electrochemical behaviour of duplex stainless steels, Wear 261 (2006) 947–953.
[6] R. Buscher, A. Fischer, The pathways of dynamic recrystallization in all-metal hip joints, Wear 259 (2005) 887–897.
[7] M. Favero, P. Stadelmann, S. Mischler, Effect of the applied potential of the near surface microstructure of a 316L steel submitted to tribocorrosion in sulfuric acid, J. Phys. D: Appl. Phys. 39 (2006) 3175–3183.
[8] A. Bidiville, M. Favero, P. Stadelmann, S. Mischler, Effect of surface chemistry on the mechanical response of metals in sliding tribocorrosion systems, Wear 263 (2007) 207–217.
[9] D.A. Rigney, Transfer, mixing and associated chemical and mechanical processes during the sliding of ductile materials, Wear 245 (2000) 1–9.
[10] I. Hutchings, Tribology: Friction and Wear of Engineering Materials, Arnold, 1992.
[11] D. Landolt, Corrosion and Surface Chemistry of Metals, EPFL Press/CRC, 2007.
[12] A. Mishra, V. Richard, F. Gregori, R.J. Asaro, M.A. Meyers, Microstructural evolution in copper processed by severe plastic deformation, Mater. Sci. Eng. A 410–411 (2005) 290–298.
[13] A. Emge, S. Karthikeyan, D.A. Rigney, The effects of sliding velocity and sliding time on nanocrystalline tribolayer development and properties in copper, Wear 267 (2009) 562–567.
[14] B. Viguier, Plasticity: recall the basic and microscopic aspects, in: B. Viguier (Ed.), Plastox 2007: Mechanisms and Mechanics of Plasticity–Environment Interactions, EDP Sciences, 2007, pp. 1–21.
[15] D. Landolt, S. Mischler, M. Stemp, Electrochemical methods in tribocorrosion: a critical appraisal, Electrochim. Acta (2001) 3913–3929.